Satellite Navigation
https://satellite-navigation.springeropen.com/

ORIGINAL ARTICLE

Open Access

Assessment of tomographic window and sampling rate effects on GNSS water vapor tomography

Fei Yang[1*], Yilin Sun[1], Xiaolin Meng[2*], Jiming Guo[3] and Xu Gong[1]

Abstract

The ground-based Global Navigation Satellite System (GNSS) water vapor tomography is increasingly important in GNSS meteorology. As the multi-GNSS and more ground-based GNSS sites can be incorporated into the regional water vapor tomographic model, determining the tomographic window and sampling rate is crucial for the modelling of the water vapor tomography. These two factors affect not only the number of available signal rays from the satellites, but also the number of tomographic voxels crossed by the signal rays. This study uses Hong Kong as the research area to explore the impact of 12 schemes with different tomographic window and sampling rate on the three water vapor tomography methods, including Least squares, Kalman filtering, and Multiplicative Algebraic Reconstruction Technique (MART). Numerical results show that the tomographic results with the three methods get better as the width of the tomographic window decreases and the sampling rate increases in these 12 schemes, and it is found that the Least squares method is most affected by the two factors, followed by Kalman filtering and MART methods. It is recommended to set a tomographic window width of 10 min and a sampling rate of 300 s in a GNSS water vapor tomographic experiment with dense GNSS site like Hong Kong.

Keywords GNSS meteorology, Water vapor, Tomography

Introduction

In Global Navigation Satellite System (GNSS) meteorology, water vapor tomography has attracted more and more attention and played increasingly a crucial role since it can accurately obtain the three-dimensional water vapor information (Yang et al., 2022a; Zhang et al., 2020). The concept of GNSS water vapor tomography was first proposed by Braun et al. (1999) and then realized by Flores et al. (2000). At present, it is one of the most powerful and accurate methods for the reconstruction of three-dimensional water vapor distribution (Sa et al., 2021; Yang et al., 2020a ; Yao et al., 2017). In tomographic approach for water vapor, a study region covered by GNSS sites is divided into a number of voxels, and the Slant Water Vapor (SWV) derived from GNSS observations passing though these voxels are used for estimating the water vapor information.

In GNSS water vapor tomography, scholars have developed different methods to solve the tomographic model, which can be mainly grouped into three types of methods, i.e. the Least squares, the Kalman filtering, and the Algebraic Reconstruction Technique (ART). Flores et al. (2000) used the Least squares approach to solve the tomographic equations by adding a set of constraints, and the method and its variates are discussed in a lot

*Correspondence:
Fei Yang
yangfei@cumtb.edu.cn
Xiaolin Meng
mengxl@bjut.edu.cn
[1] College of Geoscience and Surveying Engineering, China University of Mining and Technology-Beijing, Beijing 100083, China
[2] College of Architecture and Civil Engineering, Beijing University of Technology, Beijing 100124, China
[3] School of Geodesy and Geomatics, Wuhan University, Wuhan 430079, China

of literature (Adavi & Mashhadi-Hossainali, 2014; Shafei & Hossainali, 2020). Assuming that the Water Vapor Density (WVD) in each voxel follows the Gauss-Markov random walk pattern for a certain period of time, Gradinarsky and Jarlemark (2004) constructed the corresponding state equation and established the method of water vapor tomographic solution based on the Kalman filtering. Then the adaptive Kalman filtering and the robust Kalman filtering were proposed successively to reconstruct the water vapor information (Jiang et al., 2013; Rohm et al., 2014). Bender et al. (2011) utilized the ART that processes observation by observation to inverse the tomographic model. The Multiplicative Algebraic Reconstruction Techniques (MART) and the Simultaneous Iteration Reconstruction Techniques (SIRT) that belongs to the ART family were also adopted. (Zhang et al., 2020; Ding et al., 2020).

In these three types of water vapor tomographic methods, the number of voxels which signal rays pass through are always limited in the research region at a certain moment due to the unfavorable geometry of ground GNSS sites and fixed structure of satellites (Guo et al., 2016; Zhao et al., 2018). To realize the water vapor tomographic solution, more satellite signals need to be added to the tomographic model, that is, each water vapor tomographic solution covers a period of time. However, the water vapor content in space changes dynamically, and it is unreasonable to last for an excessively long time for a tomographic solution which can introduce more errors. Therefore, it is necessary to set the time coverage of a water vapor tomographic solution, namely the tomographic window. For a small tomographic window, it is difficult for satellite signals to cover all voxels divided in the study area. For a large tomographic window, it is hard for tomographic results to accurately reflect the changes of water vapor in space, for a large tomographic window means a long period of time during which the water vapor changes more frequently. On the other hand, the sampling rate of signal rays is another crucial parameter that needs to be determined together with the tomographic window. A slow sampling rate will reduce both the number of effective signal rays and the number of the voxels which signals pass through, while a fast sampling rate will make the signal structure in the tomographic model too similar to accurately determine the water vapor solution. The combination of tomographic window and sampling rate has different influences on the three types of water vapor tomographic methods. In the Least squares method, it directly corresponds to the number of observations and structure of the coefficient matrix of the tomographic equation, i.e., the number and distribution of the 0 elements. It influences not only both update and structure of equations, but also the period and time interval of the state and prediction update in the Kalman filter method. For the algebraic reconstruction technique, it determines the number and frequency of iterative calculations for a voxel.

In the current research, the water vapor tomographic window and the sampling rate are selected empirically, and no related principles and standard can be refereed to. The tomographic window is often set to 30 min in some studies because the water vapor density during this period can be assumed constant (Brenot et al., 2019; Liu et al., 2019; Zhao et al., 2019). For the sampling rate, it is only mentioned in some papers, such as Benevides et al. (2018) adopted the sampling rate of 30 s in the Lisbon experiment and Ding et al. (2018) utilized the sampling rate of 300 s in the Hong Kong experiment. Therefore, this paper attempts to explore the effects of a combination of tomographic window and sampling rate on GNSS water vapor tomography. In these experiments, the three types of tomographic methods are adopted and compared for their performances based on different combinations.

Methodology

Tomographic observation equation

The SWV is used as observation in the GNSS water vapor tomography, which can be converted from Slant Wet Delay (SWD) by using the following formula (Adavi & Mashhadi, 2015):

$$d_{\mathrm{SWV}} = \frac{1 \times 10^6}{\rho_w \times \frac{R}{m_w}\left(\frac{k_3}{T_m} + k_2 - \frac{m_w}{m_d} \times k_1\right)} \times d_{\mathrm{SWD}} \tag{1}$$

where ρ_w denotes the liquid water density, R is the universal gas constant, k_1, k_2 and k_3 are the empirical physical constants, m_d and m_w represent the molar mass of the dry and the wet atmosphere (Yang et al., 2022b), and T_m is weighted mean temperature that can be computed with surface temperature using Bevis formula (Bevis et al., 1992; Huang et al., 2019; Yang et al., 2020b, 2022c). The d_{SWD} can be obtained by mapping the Zenith Wet Delay (ZWD) and the wet delay gradients into the zenith direction using the following formula:

$$\begin{aligned} d_{\mathrm{SWD}} = {} & f(\beta_{\mathrm{ele}}) \times d_{\mathrm{ZWD}} + f(\beta_{\mathrm{ele}}) \times \cot(\beta_{\mathrm{ele}}) \\ & \times \left(G^w_{\mathrm{NS}} \times \cos(\beta_{\mathrm{azi}}) + G^w_{\mathrm{WE}} \times \sin(\beta_{\mathrm{azi}})\right) \end{aligned} \tag{2}$$

where β_{ele} and β_{azi} represent the elevation and azimuth angles of a satellite, respectively; f refers to the wet mapping function; G^w_{NS} and G^w_{WE} denote the wet delay

gradient parameters in the north–south and east–west direction, respectively. After retrieving the Zenith Total Delay (ZTD) from GNSS data processing, the ZWD is separated from ZTD by subtracting the Zenith Hydrostatic Delay (ZHD) (Yang et al., 2021; Zhao et al., 2021), which can be calculated with the Saastamoinen model using the pressure as follows:

$$d_{\mathrm{ZHD}} = \frac{0.002\,277 \times P_s}{1 - 0.002\,66 \times \cos(2\varphi) - 0.000\,28 \times h} \tag{3}$$

where P_s represent the measured surface pressure, φ and h are the latitude and geodetic height of the GNSS sites, respectively.

After discretizing the tomographic region into finite voxels according to its latitude, longitude, and altitude, the distances of GNSS signal rays crossing the voxels need to be calculated by ray tracing its path from receiver to satellite. Then the observation equation of GNSS water vapor tomography can be expressed as the following formula:

$$d^p_{\mathrm{SWV}} = \sum_{i=1}^{n} d^p_i \cdot x_i \tag{4}$$

where the superscript p denotes the index of the satellite signal rays, n refers to the total number of the voxels discretized in the tomographic region, d^p_i represents the distance of the pth signal ray passing voxel i, and x_i is the ith unknown parameter, namely the water vapor density in voxel i.

The Least squares method

Two types of constraints are usually added into the tomographic equation in the Least squares method as follows:

$$\boldsymbol{O} = \boldsymbol{H} \cdot \boldsymbol{x} \tag{5}$$

$$\boldsymbol{O} = \boldsymbol{V} \cdot \boldsymbol{x} \tag{6}$$

where Eqs. (5) and (6) represent the horizontal and vertical constraints, respectively. $\boldsymbol{H}$ and $\boldsymbol{V}$ denote the coefficient matrix for the two types of constraints, $\boldsymbol{O}$ denotes zero matrix, $\boldsymbol{x}$ denotes unknown parameter matrix.

Based on the assumption that the distribution of water vapor density is relatively stable in the horizontal direction, the horizontal constraints are always represented by the weighted average of its neighboring voxels in the same layers (Zhao et al., 2018). For the vertical constraints, it is an exponential relationship for the water vapor density of the voxels between two adjacent layers based on the analysis of the meteorological profile for many years (Yang et al., 2022a). Then the water vapor tomographic solution can be achieved according to the principle of the Least squares as the following formula:

$$\hat{\boldsymbol{x}} = \left(\boldsymbol{A}^{\mathrm{T}}\boldsymbol{P}\boldsymbol{A} + \boldsymbol{H}^{\mathrm{T}}\boldsymbol{P}_H\boldsymbol{H} + \boldsymbol{V}^{\mathrm{T}}\boldsymbol{P}_V\boldsymbol{V}\right)^{-1} \times \left(\boldsymbol{A}^{\mathrm{T}}\boldsymbol{P}\boldsymbol{y}\right) \tag{7}$$

where $\boldsymbol{A}$ represents the coefficient matrix of the observation equations, $\boldsymbol{y}$ denotes the column vector of SWV. $\boldsymbol{P}, \boldsymbol{P}_H, \boldsymbol{P}_V$ are the weighting matrix for the observation equation, the horizontal constraint equation, and the vertical constraint equation, respectively.

The Kalman filtering method

Based on the principle of minimum mean squared error in the estimation, this method separates the observations and process (Jiang et al., 2013). The process represents the water vapor density evolutes with time, which is expressed as a liner dynamic system (Rohm et al., 2014):

$$\overline{\boldsymbol{x}}_{k+1} = \boldsymbol{\Phi}_k \cdot \boldsymbol{x}_k + \boldsymbol{\omega}_k \tag{8}$$

where $\boldsymbol{x}_k$ is the water vapor density at epoch k, $\overline{\boldsymbol{x}}_{k+1}$ refers to the estimated water vapor density at epoch $k+1$. $\boldsymbol{\Phi}_k$ is a state transition matrix, $\boldsymbol{\omega}_k$ denotes the dynamic disturbance noise matrix and its covariance matrix is $\boldsymbol{Q}_k$. The linear observation model at epoch $k+1$ is as follows:

$$\boldsymbol{d}^{\mathrm{SWV}}_{k+1} = \boldsymbol{A}_{k+1} \cdot \boldsymbol{x}_{k+1} + \boldsymbol{\Delta}_{k+1} \tag{9}$$

where $\boldsymbol{A}_{k+1}$ represents the coefficient matrix of the distances in the crossed voxels at epoch $k+1$, $\boldsymbol{\Delta}_{k+1}$ is the observation noise matrix and its covariance matrix is $\boldsymbol{R}_{k+1}$. The prediction step of Kalman filtering is given as:

$$\overline{\boldsymbol{P}}_{k+1} = \boldsymbol{\Phi}_k \cdot \boldsymbol{P}_k \cdot \boldsymbol{\Phi}_k + \boldsymbol{Q}_k \tag{10}$$

where $\boldsymbol{P}_k$ and $\overline{\boldsymbol{P}}_{k+1}$ are the prediction and correction of the covariance matrix of the estimated state. Then the estimated state can be corrected, and the covariance matrix is updated as follows (Zhang et al., 2008):

$$\boldsymbol{x}_{k+1} = \overline{\boldsymbol{x}}_{k+1} + \boldsymbol{G}\left(\boldsymbol{d}^{\mathrm{SWV}}_{k+1} - \boldsymbol{A}_{k+1} \cdot \overline{\boldsymbol{x}}_{k+1}\right) \tag{11}$$

$$\boldsymbol{P}_{k+1} = (\boldsymbol{I} - \boldsymbol{G}\boldsymbol{A}) \cdot \overline{\boldsymbol{P}}_{k+1} \tag{12}$$

where I denotes the unit matrix. G is the Kalman gain matrix, which can be calculated as follows:

$$\boldsymbol{G} = \overline{\boldsymbol{P}}_{k+1}\boldsymbol{A}^{\mathrm{T}}\left(\boldsymbol{A}\overline{\boldsymbol{P}}_{k+1}\boldsymbol{A}^{\mathrm{T}} + \boldsymbol{R}\right)^{-1} \tag{13}$$

The algebraic reconstruction technique

The algebraic reconstruction technique is based on the application of corrections estimated from the residuals between the reconstructed and observed quantity, which iterate over the initial estimate until a certain condition

is satisfied (Bender et al., 2011). Three types of ARTs, including the traditional ART, MART, and SIRT, are applied in water vapor tomography according to the way how these corrections are computed.

Based on the assumption that there is a linear relationship between the values to be reconstructed and the projected values for each voxel, the water vapor density of voxels are corrected in ART as follows (Yu et al., 2016):

$$\tilde{x}_j^{k+1} = \tilde{x}_j^k + \lambda a_{ij} \frac{d_i^{\mathrm{SWV}} - \sum_{j=1}^{n} a_{ij}\tilde{x}_j^k}{\sum_{j=1}^{n} a_{ij}^2} \tag{14}$$

where $\tilde{x}_j^k$ denotes the water vapor density in voxel j for the kth iteration, n is the number of columns of the tomographic observation equation, a_{ij} is the element in the row i and column j of matrix $\boldsymbol{A}$, and λ is the relaxation parameter. The MART and SIRT are expressed as the following formulas (Zhang et al., 2020):

$$\tilde{x}_j^{k+1} = \tilde{x}_j^k \left(\frac{d_i^{\mathrm{SWV}}}{\sum_{j=1}^{n} a_{ij}\tilde{x}_j^k} \right)^{\frac{\lambda a_{ij}}{\sum_{j=1}^{n} a_{ij}^2}} \tag{15}$$

$$\tilde{x}_j^{k+1} = \tilde{x}_j^k + \lambda \sum_{i=1}^{m} \frac{a_{ij}\left(d_i^{\mathrm{SWV}} - \sum_{j=1}^{n} a_{ij}\tilde{x}_j^k \right)}{\sum_{j=1}^{n} a_{ij}^2} \tag{16}$$

where m is the total number of signal rays adopted in the tomographic model. The other parameters are as Eq. (14). Note that the MART is the most used iterative reconstruction technique for water vapor tomography, which is also utilized in this study.

Experiment and analysis

In this experiment, the Hong Kong satellite Positioning Reference Station Network (SatRef) was used, which covers the latitude from 22.19 to 22.54°N, the longitude from 113.87 to 114.35°E, and the altitude of tomographic area is from 0 to 8 km. The study area was divided into 560 voxels with 10 layers in the vertical direction and 8×7 in the horizontal direction. As shown in Fig. 1, 14 GNSS sites were adopted in this experiment, of which 13 sites were used to provide SWV values for tomography modeling. The GNSS site HKQT along with a radiosonde site (45,004) was selected to assess the results of water vapor tomography.

To accurately obtain the GNSS SWV, the GNSS observation data including Global Positioning System (GPS), GLObal NAvigation Satellite System (GLONASS), Galileo navigation satellite system (Galileo) and BeiDou Navigation Satellite System (BDS) from Day of Year (DOY) 152 to 181, 2021 were processed using software GAMIT 10.71 based on a double-differenced model, which estimated the tropospheric parameters including ZTD and gradient parameters. Three International GNSS Service (IGS) sites, JFNG, LHAZ, and URUM, were included in data processing to weaken the correlation of tropospheric parameters due to the short baselines within Hong Kong. The sampling rate of the observations was 30 s, a cut-off elevation angle of 10° was selected, and the orbit and clock products for multi-constellations from Center for Orbit Determination in Europe (CODE) were adopted. The LC_AUTCLN and BASELINE modes were adopted as the processing strategies, meaning that the GNSS observations were the ionosphere-free linear combination, and the orbital parameters were fixed. Note that the ZHD values were achieved using the measured surface pressure recorded by automatic meteorological device based on Saastamoinen model. To explore the influences of these two factors on the water vapor tomography using the three types of methods, twelve schemes with different tomographic windows and different sampling rates were selected in this experiment. Specifically, the tomographic windows were set to 30 min, 20 min, 10 min, and the sampling rates were set to 30 s, 60 s, 150 s, 300 s, respectively. For each scheme, different results of water vapor tomography were achieved and compared using the three types of tomographic methods.

The number of satellite signal rays available in each tomographic solution is counted for these 12 schemes, and the boxplots for the whole month are showed in Fig. 2. The tomographic window and sampling rate have a great influence on the number of available signal rays. It gets significantly larger as the window width increases, and it decreases obviously as the sampling rate increases. The boxplots also reflect the fluctuation of the number of available signal rays, which also conforms the above rule. The scheme with the window width of 30 min and sampling rate of 30 s has the largest number of available signal rays with a median value of 16,990, and the scheme with the window width of 10 min and sampling rate of 300 s has the smallest number of available signal rays with a median value of 836. Note that the number of available signal rays in the following schemes is equivalent, i.e., the scheme with the window width of 10 min and sampling rate of 30 s and the scheme with the window width of 20 min and sampling rate of 60 s; the scheme with the window width of 20 min and sampling rate of 300 s and

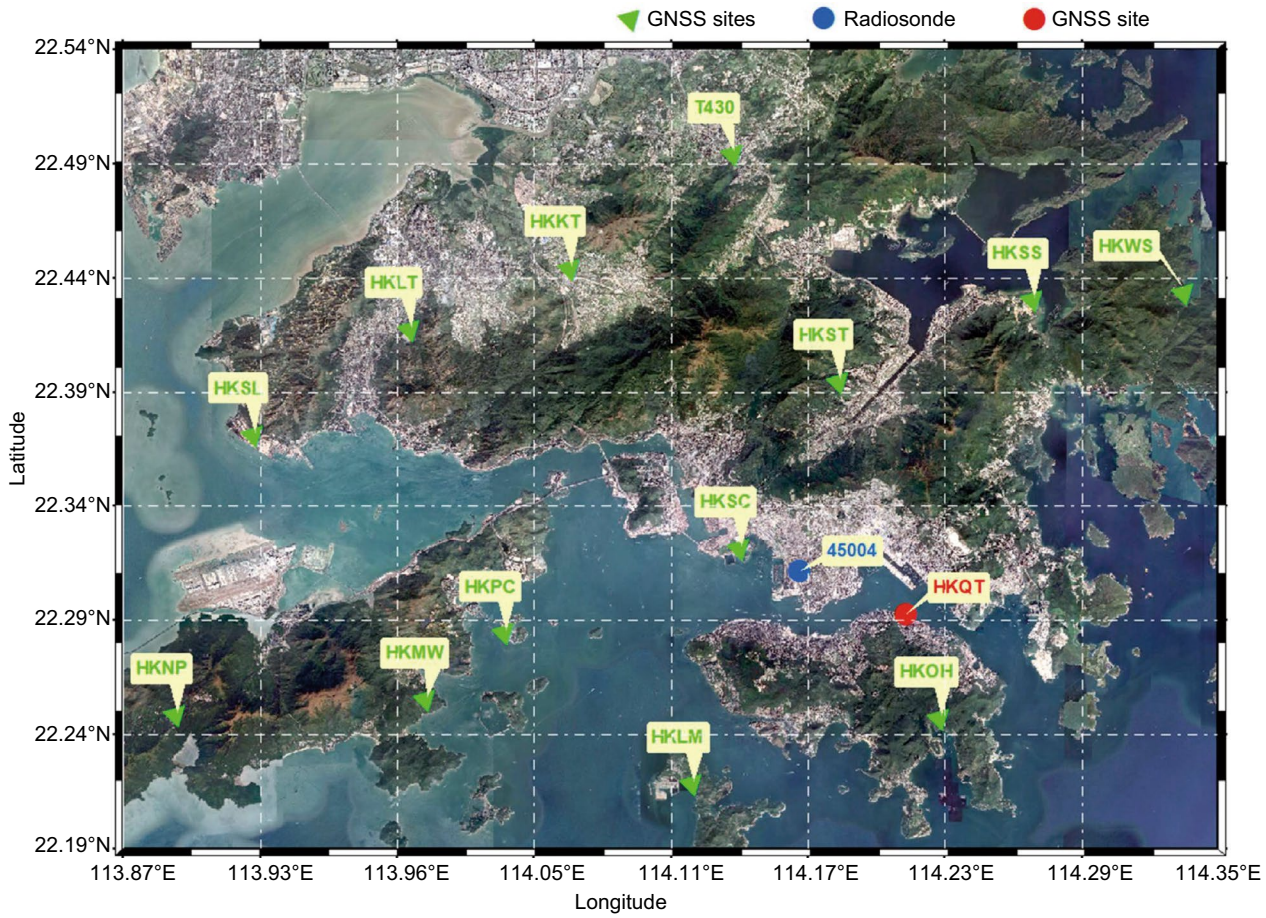

Fig. 1 Distribution of GNSS and radiosonde sites and the horizontal structure of the voxels

the scheme with the window width of 10 min and sampling rate of 150 s.

The number of voxels passed through by signal ray, which is more important than the number of signal rays available, is also counted for these 12 schemes. The statistics of the eight selected days are shown in Fig. 3, where the shapes and colors represent the different tomographic windows and sampling rates. One can see that the number of voxels crossed by signal rays is also affected by the tomographic window and the sampling rate, that is, the larger the window and the faster the sampling rate, the higher the number of available signal rays will be. However, this effect is not obvious. As can be seen from Table 1, which lists the average number of voxels passed through by signal rays during the month, the mean values are 475, 475, 474 and 472 for the schemes with sampling rate of 30 s, 60 s, 150 s, and 300 s, respectively. When the tomographic window changes to 20 min and 10 min, these values are 469/469/468/466 and 458/458/457/456, respectively. It indicates that the change of sampling rate cannot effectively increase the number of the voxels crossed by signal rays when the tomographic window is fixed. On the other hand, the coverage rate of voxels passed through by signal rays is increased by 1.95% for the tomographic window from 10 to 20 min when the sampling rate is fixed. This value becomes to 2.98% when the tomographic window is changed to 30 min. This illustrates that it is not an efficient method to increase the number of voxels passed through by signal rays by directly expanding the tomographic window.

Tomographic results

To assess the influence of these 12 schemes on different tomographic methods in water vapor tomography, SWV values at the site HKQT were computed using these tomographic results based on the observation equation in Eq. (4). This type of SWV is called as tomography-computed SWV, which are compared with the GAMIT-estimated SWV (as reference). The changes of tomography-computed versus GAMIT-estimated SWV

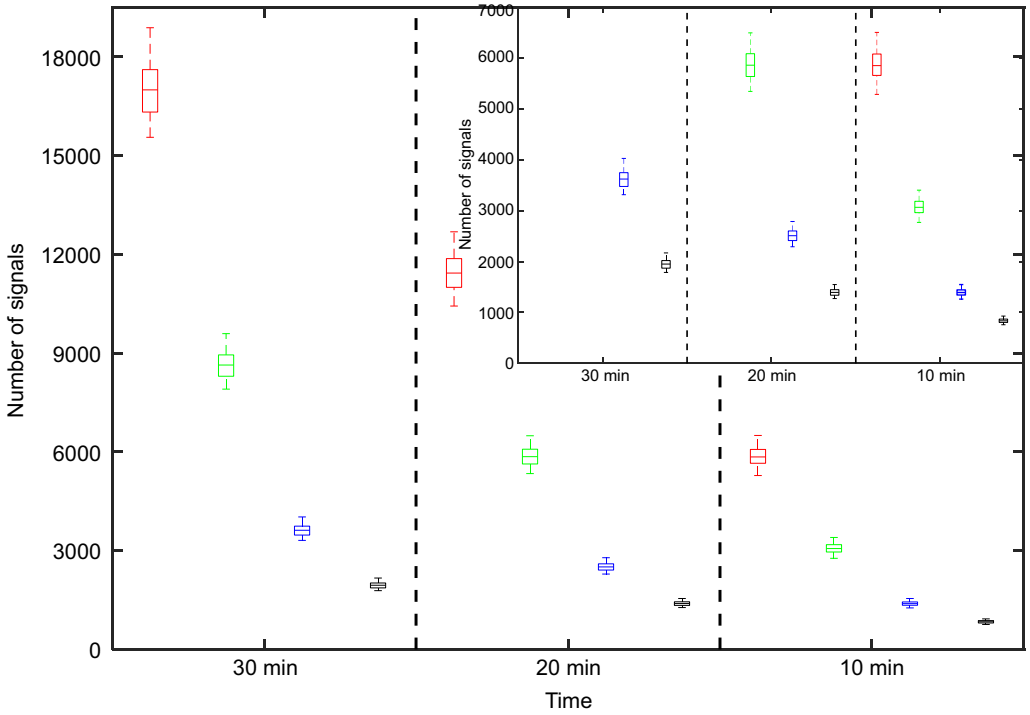

Fig. 2 Boxplot of the number of available signal rays for each scheme (red, green, blue, and blank represent the sampling rate of 30 s, 60 s, 150 s and 300 s, respectively)

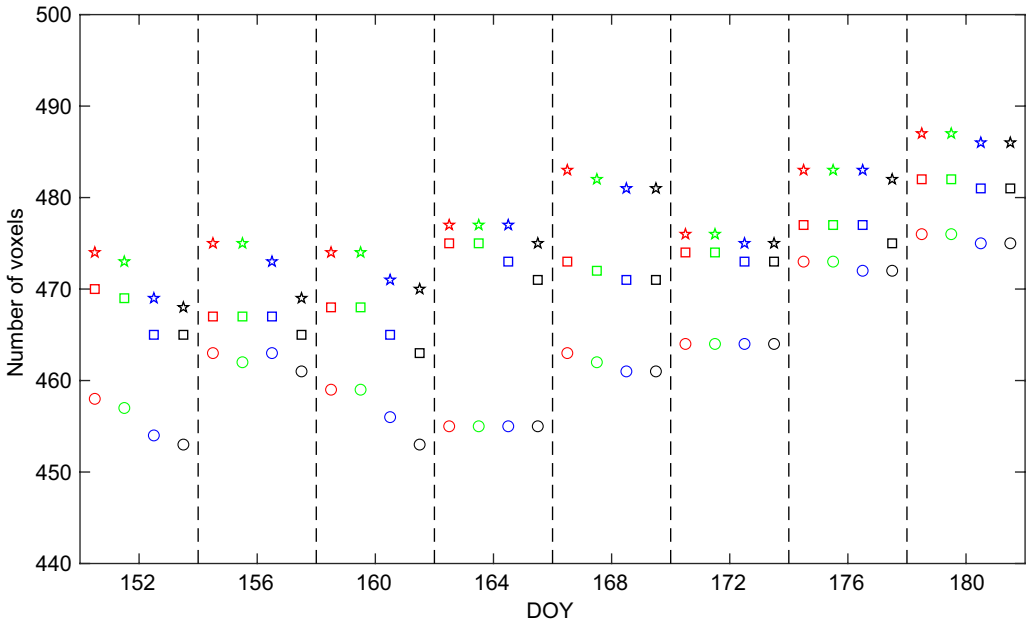

Fig. 3 Number of the voxels passed through by signal rays in each solution for each scheme in the eight selected days (pentagram, square, and circle denote the tomographic window of 30 min, 20 min and 10 min, respectively; red, green, blue, and blank represent the sampling rate of 30 s, 60 s, 150 s and 300 s, respectively)

Table 1 Statistics of the voxels crossed by signal rays for each scheme

Tomographic window (min)	Sampling rate (s)	Average number	Coverage rate (%)
30	30	475	84.8
	60	475	84.8
	150	474	84.6
	300	472	84.3
20	30	469	83.8
	60	469	83.8
	150	468	83.6
	300	466	83.2
10	30	458	81.8
	60	458	81.8
	150	457	81.6
	300	456	81.4

residuals with elevation angles during the experimental period are illustrated in Fig. 4, in which colors denote the three tomographic method and each panel represent one scheme.

It is observed that the SWV residuals of all tomographic results have the same trend, that is, they decrease as the elevation angle increases. The SWV residuals range from −10 to 10 mm and most of them are concentrated between −2.0 and 2.0 mm for these 12 schemes based on the three methods. The schemes with different tomographic window widths and sampling rates have different influence on the three tomographic methods. The effect is relatively small for MART and relatively large for the Least squares and the Kalman filtering. The large residuals of the results can be seen in the schemes with slow sampling rate for the Least Squares and Kalman filter. This may be because the satellite signals at adjacent epochs often pass through the same voxels, thus making the row vectors in the coefficient matrix of the observation equation similar, which easily leads to the instability of the solution using the least squares method and the Kalman filter. Moreover, the performances of these three methods are gradually improved with the tomographic window width decreasing and the sampling rate increasing. For the schemes with the tomographic window width of 30 min, the SWV residuals derived from the Kalman filtering and the Least squares are improved when the

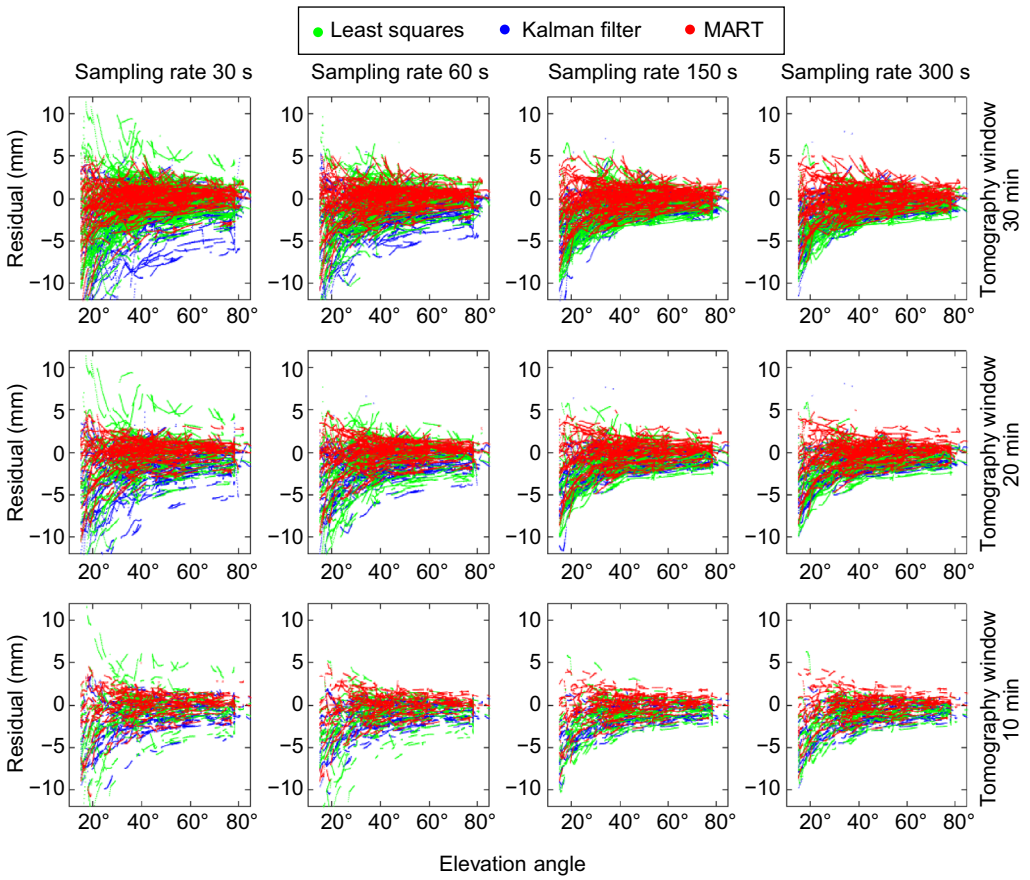

Fig. 4 Scatter diagram of the change of SWV residuals with elevation angle in three types of methods for different schemes

sampling rate extends from 30 to 300 s. The above phenomenon can also be found in other comparisons with the tomographic window width fixed. For the schemes with the sampling rate of 30 s, the SWV residuals derived with the Kalman filtering and the Least squares are also improved when the tomographic window width decreases from 30 to 10 min. The above phenomenon is no longer significant for the schemes with slow sampling rate. For example, when the sampling rate is 30 s, the Root Mean Square Error (RMSE) of the SWV residuals is 3.71 mm based on the Least squares for the scheme with the tomographic window width of 30 min and the values changes to 2.25 mm for the scheme with the tomographic window width of 10 min. But when the sampling rate is fixed at 300 s, the RMSE of the SWV residuals is 1.89 mm and 1.79 mm for these two tomographic windows.

Further, the SWV results of each tomographic solution were compared, and their RMSE distributions are shown in the form of boxplot in Fig. 5, which also illustrates the impact of the different schemes on these methods. It indicates that the tomographic window width and the sampling rates have obvious impact on the results of the Least squares and the Kalman filtering methods, but less impact on the results of MART, which are consistent with the phenomenon in Fig. 4. From the panels in the same row, the ranges of fluctuations and extreme values derived with the Least squares and the Kalman filtering methods become smaller in each tomographic window as the sampling rate increases. From the panels in the same column, the ranges of extreme values derived with the Least squares and the Kalman filtering methods do not change much as the tomographic window width decreases, while the improvement of the fluctuations can still be observed. For the MART, its results do not differ much in these 12 tomographic schemes. Specifically, in the schemes with tomographic window width of 10 min and sampling rate of 300 s, the three methods achieve the mean RMSE of 1.79 mm, 1.73 mm, and 1.50 mm, respectively.

Radiosonde provides a primary source of upper-air data, which is used to calculate the water vapor density profile with high accuracy. In this section, the water vapor density derived from the radiosonde at 45,004 is used as a reference value to assess the tomographic results with different tomographic methods based on these 12 schemes. The water vapor density on DOY 152 is compared between radiosonde data and tomographic results, and Fig. 6 shows the situations for these 12

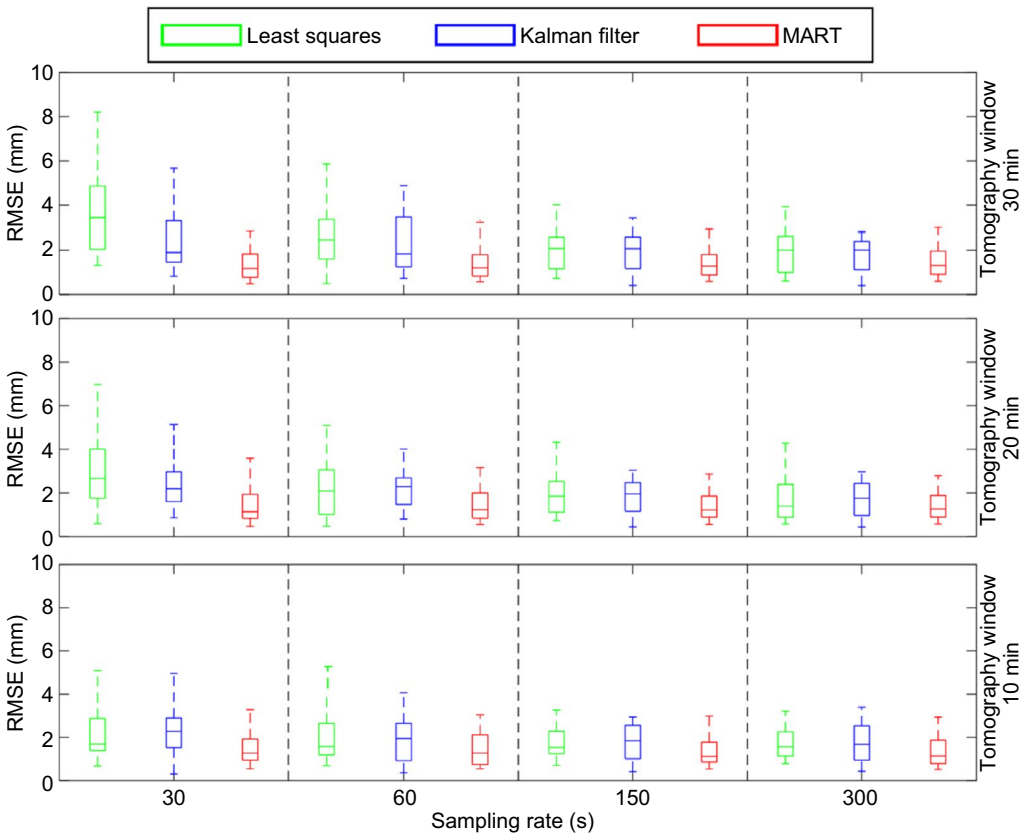

Fig. 5 Boxplot of the SWV RMSEs in three types of methods for different schemes during the experimental period

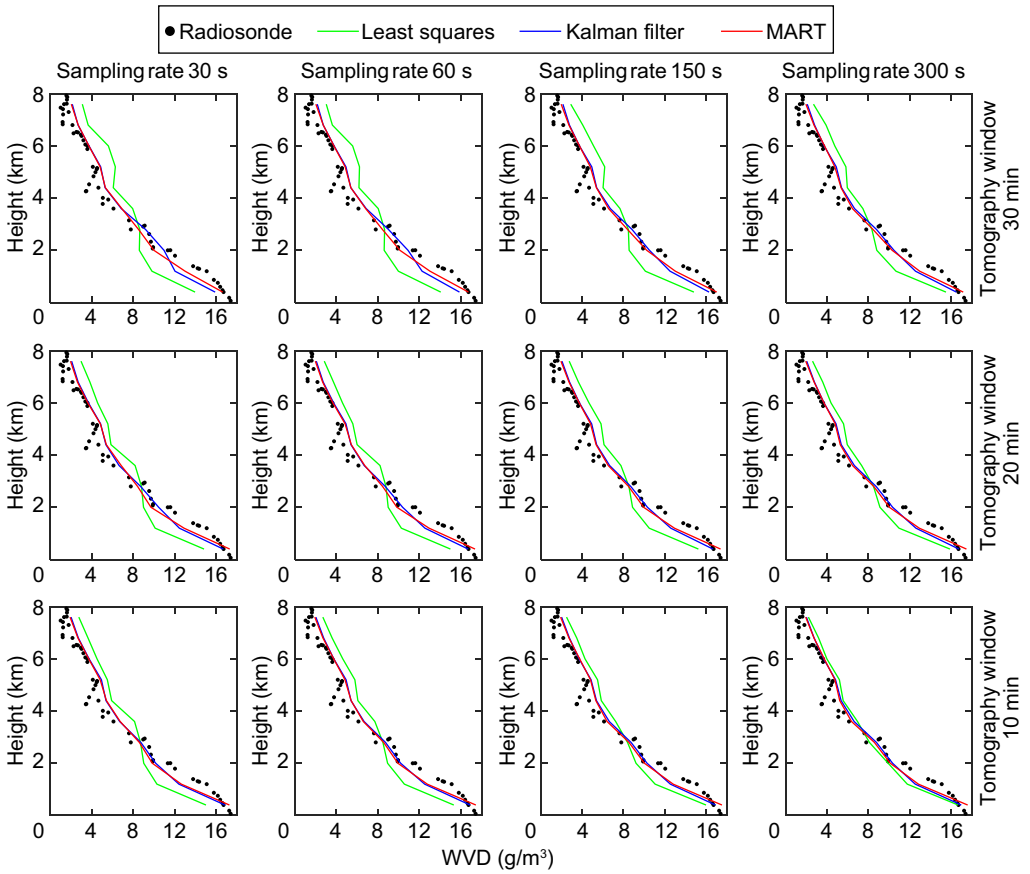

Fig. 6 water vapor density comparison between radiosonde data and the three tomographic methods in different schemes

schemes with different tomographic methods. It is clearly from the profiles that the water vapor density decreases with increasing height. The tomographic results with the three methods in different schemes are consistent with this trend, but the obvious differences with the true values are observed in different schemes. From the 12 panels in Fig. 6, the green curves change most, showing that the tomographic window width and sampling rate have the greatest influence on the tomographic results with the Least squares. Specifically, the water vapor density reconstructed with the Least squares method are more consistent with that derived from radiosonde data as the tomographic window width decreases and the sampling rate increases. The influences of the tomographic window width and sampling rate on the other tomographic methods are relatively little, especially on the MART. When the tomographic window width is 10 min and the sampling rate is 300 s, the water vapor density reconstructed with these three methods is consistent with each other. Moreover, the mean RMSEs of WVD are listed in Table 2, which shows the same conclusions as Fig. 6.

To explore the overall accuracy of water vapor density reconstructed with the three methods, all the WVD results during the experimental period are compared with those derived from radiosonde data, and the correlations are illustrated in Fig. 7. The scatter points of the three colors in the 12 panels are close to the 1:1

Table 2 Mean RMSE of WVD for the three tomographic methods in different schemes (g/m^3)

Tomographic window (min)	Sampling rate (s)	Least squares	Kalman filtering	MART
30	30	3.45	2.31	1.80
	60	2.88	1.89	1.69
	150	2.38	1.68	1.65
	300	1.79	1.65	1.64
20	30	2.71	2.04	1.73
	60	2.42	1.78	1.72
	150	1.94	1.67	1.65
	300	1.70	1.66	1.64
10	30	2.21	1.83	1.69
	60	1.94	1.71	1.67
	150	1.69	1.66	1.64
	300	1.65	1.65	1.64

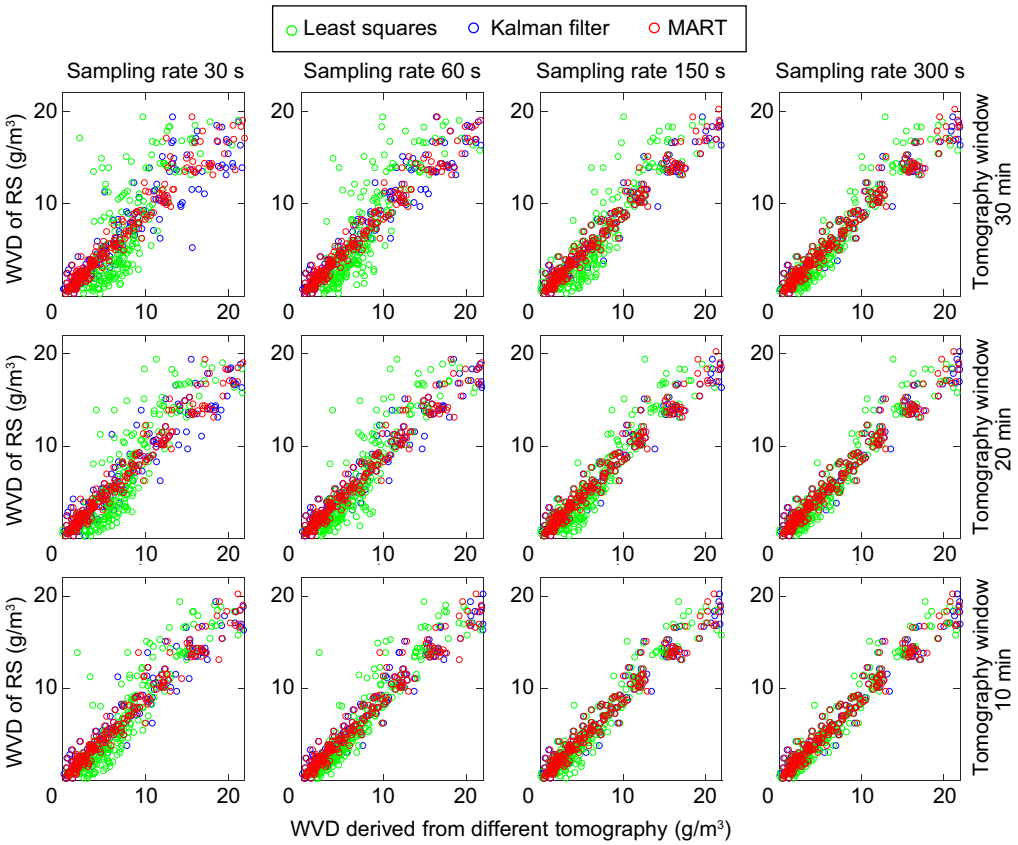

Fig. 7 Correlation of the WVD reconstructed with three tomographic methods and those derived from the radiosonde data in these 12 schemes

line, with the red performing the best in most cases followed by the blue and green. As the tomographic window width decreases and the sampling rate decreases, the WVD results reconstructed with the Least squares and the Kalman filtering methods are getting closer to those with MART. The correlation coefficient between the WVD reconstructed with MART and those derived from the radiosonde data is 0.98 in 11 schemes and 0.97 in the scheme with tomographic window width of 30 min and sampling rate of 30 s. For the Kalman filtering, its correlation coefficients are relatively small in the schemes with low sampling rate, i.e., 0.94 for the scheme with tomographic window width of 30 min and sampling rate of 30 s, 0.96 for the scheme with tomographic window width of 20 min and sampling rate of 30 s, 0.97 for the scheme with tomographic window width of 30 min and sampling rate of 60 s, 0.97 for the scheme with tomographic window width of 20 min and sampling rate of 60 s, and 0.97 for the scheme with tomographic window width of 10 min and sampling rate of 30 s. And the correlation coefficients of other schemes all reach 0.98. For the Least Squares method, the correlation coefficients are 0.75/0.83/0.89/0.95, 0.86/0.89/0.94/0.96, and 0.91/0.93/0.96/0.97, respectively. Note that the correlation coefficient is obviously improved with the increase of sampling rate, and the coefficient also reach the level of the other two tomographic methods in the scheme with tomographic window width of 10 min and sampling rate of 300 s.

Discussion and conclusions

In this paper, the influences of tomographic window width and sampling rate on the water vapor tomography are analyzed in detail using the Hong Kong SatRef as the research area. These two factors directly affect the number of available signals and voxels crossed by GNSS signal rays. Three tomographic methods, i.e., the Least squares, the Kalman filtering, and MART are utilized to conduct the experiments in 12 schemes with different windows widths and sampling rates. The SWV estimated by GAMIT software and WVD derived from radiosonde data are used as references to investigate the differences of the three methods under these 12 schemes.

Numerical results show that the tomographic window width and sampling rate can effectively increase the number of available satellite rays, but the increase in the number of voxels crossed by signal rays is very limited. The two factors have the same effect on the

tomographic results with the three methods, that is, all the tomographic results get better as the tomographic window width decreases and the sampling rate increases. It also indicates that the number of voxels passed by signal rays is more important than the number of available signal rays in water vapor tomography. The Least squares method is most affected by the above two factors. Its tomographic results will be poor when the tomographic window width is large and the sampling rate is fast, and it will also achieve good tomographic results in the schemes with a small tomographic window and a slow sampling rate. This is because the coefficient matrix of the observation equations needs to be solved in the Least squares, such as the operation of matrix inversion. The larger tomographic window and a faster sampling rate will increase the number of observations, but the coefficient matrix is highly correlated and becomes very large with most of the elements being 0, which leads to more uncertainties in the inversion of water vapor. The Kalman filtering method is less affected by these two factors, but the poor tomographic results are still observed in the schemes with large tomographic window and fast sampling rate. This is due to that an appropriate time period and interval are required for the prediction and updating in the Kalman filtering. For the MART, these two factors have almost no effect on its tomographic results, which illustrates that the iterative reconstruction technique is stable in the water vapor tomography. Note that smaller tomographic window and slower sampling rate are more conducive to acquire the water vapor information with high efficiency for MART. In Hong Kong with dense GNSS sites in this experiment, it is recommended to set a tomographic window width of 10 min and a sampling rate of 300 s in the water vapor tomography no matter which tomographic method is used.

In the follow-up research, it is necessary to take into consideration the distribution and density of GNSS sites, the number of available satellite systems, and the influence of the weather condition on the change in water vapor to find more suitable tomographic windows and sampling rates for a specific region. In addition, more attentions should be paid to the inclusion of the satellite signals from the side face of the tomographic research, the fusion of the data derived from the meteorological remote sensing satellite (e.g., MODIS and FengYun), and the discussion of the optimal weight of the multi-source data, to continuously improve the accuracy of the GNSS water vapor tomography.

Acknowledgements
The authors would like to thank Hong Kong Geodetic Survey Services for providing the data of SatRef. We thank all anonymous reviewers for their valuable, constructive, and prompt comments.

Author contributions
Conceptualization, FY and XM; methodology, FY and YS; data curation, JG, XM and XG; validation, FY, YS and XG; formal analysis, FY; resources, JG and XM; writing—original draft preparation, FY; writing—review and editing, FY, XM, JG, YS and XG. All authors read and approved the final manuscript.

Funding
This study is supported by Beijing Natural Science Foundation (No. 8224093), China Postdoctoral Science Foundation (No. 2021M703510), Fundamental Research Funds for the Central Universities (No. 2021XJDC01), Key Laboratory of South China Sea Meteorological Disaster Prevention and Mitigation of Hainan Province (No. SCSF202109), Open Fund of State Key Laboratory of Geodesy and Earth's Dynamics Innovation Academy for Precision Measurement Science and Technology (No. SKLGED2022-3–1), Beijing Key Laboratory of Urban Spatial Information Engineering (No. 20220117), and the National Natural Science Foundation of China (No. 42204022).

Availability of data and materials
The data used in this study are available from the corresponding author upon request.

Declarations

Competing interests
The authors declare that they have no conflict of interest.

Received: 23 September 2022 Accepted: 12 January 2023
Published online: 20 February 2023

References

Adavi, Z., & Mashhadi-Hossainali, M. (2014). 4D tomographic reconstruction of the tropospheric wet refractivity using the concept of virtual reference station, case study: Northwest of Iran. *Meteorology and Atmospheric Physics., 126*(3–4), 193–205.

Adavi, Z., & Mashhadi-Hossainali, M. (2015). 4D-tomographic reconstruction of water vapor using the hybrid regularization technique with application to the North West of Iran. *Advances in Space Research., 55*, 1845–1854.

Bender, M., Dick, G., Ge, M., Deng, Z., Wickert, J., Kahle, H., Raabe, A., & Tetzlaff, G. (2011). Development of a GNSS water vapour tomography system using algebraic reconstruction techniques. *Advances in Space Research., 47*(10), 1704–1720.

Benevides, P., Catalao, J., Nico, G., & Miranda, P. (2018). 4D wet refractivity estimation in the atmosphere using GNSS tomography initialized by radiosonde and AIRS measurements: Results from a 1-week intensive campaign. *GPS Solutions, 22*, 91.

Bevis, M., Businger, S., Herring, T., Rocken, C., Anthes, R., & Ware, R. (1992). GPS meteorology: Remote sensing of atmospheric water vapor using the global positioning system. *Journal of Geophysical Research Atmosphere., 97*(D14), 15787–15801.

Braun, J., Rocken, C., Meetrens, C., & Ware, R. (1999). Development of a water vapor tomography system using low cost L1 GPS receivers. 9th ARM science team meeting, US Department of Energy, San Antonio, Texas, 22–26 March.

Brenot, H., Rohm, W., Moller, G., Rapant, L., Biondi, R., Manning, T., & Champollion, C. (2019). Cross-comparison and methodological improvement in GPS tomography. *Remote Sensing., 12*, 30.

Ding, N., Yan, X., Zhang, S., Wu, S., Wang, X., Zhang, Y., Wang, Y., Liu, X., Zhang, W., Holden, L., & Zhang, K. (2020). Node-based optimization of GNSS tomography with a minimum bounding box algorithm. *Remote Sensing., 12*, 2744.

Ding, N., Zhang, S., Wu, S., Wang, X., & Zhang, K. (2018). Adaptive node parameterization for dynamic determination of boundaries and nodes of GNSS tomographic models. *Journal of Geophysical Research: Atmosphere., 123*, 1990–2003.

Flores, A., Ruffini, G., & Rius, A. (2000). 4D tropospheric tomography using GPS slant wet delays. *Annales Geophysicae., 18*(2), 223–234.

Gradinarsky, L., & Jarlemark, P. (2004). Ground-based GPS tomography of water vapor: Analysis of simulated and real data. *Journal of the Meteorological Society of Japan., 82*(1B), 551–560.
Guo, J., Yang, F., Shi, J., & Xu, C. (2016). An optimal weighting method of global positioning system (GPS) troposphere tomography. *IEEE Journal of Selected Topics in Applied Earth Observations and Remote Sensing., 12*, 5880–5887.
Huang, L., Jiang, W., Liu, L., Chen, H., & Ye, S. (2019). A new global grid model for the determination of atmospheric weighted mean temperature in GPS precipitable water vapor. *Journal of Geodesy, 93*(2), 159–176.
Jiang, P., Ye, S., He, S., & Liu, Y. (2013). Ground-based GPS tomography of wet refractivity with adaptive Kalman filter. *Geomatics and Information Science of Wuhan University., 38*(3), 299–302.
Liu, W., Lou, Y., Zhang, W., Huang, J., Zhou, Y., & Zhang, H. (2019). On the study of influences of different factors on the rapid tropospheric tomography. *Remote Sensing., 11*, 1545.
Rohm, W., Zhang, K., & Bosy, J. (2014). Limited constraint, robust Kalman filtering for GNSS troposphere tomography. *Atmospheric Measurement Technique., 7*(5), 1475–1486.
Sa, A., Rohm, W., Fernandes, R., Trzcina, E., Bos, M., & Bento, F. (2021). Approach to leveraging real-time GNSS tomography usage. *Journal of Geodesy., 95*(1), 1–21.
Shafei, M., & Hossainali, M. (2020). Application of the GPS reflected signals in tomographic reconstruction of the wet refractivity in Italy. *Journal of Atmospheric and Solar-Terrestrial Physics., 207*, 105348.
Yang, F., Guo, J., Chen, M., & Zhang, D. (2022a). Establishment and analysis of a refinement method for the GNSS empirical weighted mean temperature model. *Acta Geodaetica Et Cartographica Sinica., 51*(11), 2339–2345.
Yang, F., Guo, J., Meng, X., Shi, J., Zhang, D., & Zhao, Y. (2020b). An improved weighted mean temperature (Tm) model based on GPT2w with Tm lapse rate. *GPS Solutions, 24*, 46.
Yang, F., Guo, J., Shi, J., Meng, X., Zhao, Y., Zhou, L., & Zhang, D. (2020a). A GPS water vapor tomography method based on a genetic algorithm. *Atmospheric Measurement Techniques., 13*, 355–371.
Yang, F., Meng, X., Guo, J., Yuan, D., & Chen, M. (2021). Development and evaluation of the refined zenith tropospheric delay (ZTD) models. *Satellite Navigation., 2*, 21.
Yang, F., Wang, J., Wang, H., Hong, X., Wang, L., & Huang, B. (2022b). Assessment of the water vapor tomography based on four navigation satellite systems and their various combinations. *Remote Sensing., 14*, 3552.
Yang, F., Wang, L., Li, Z., Tang, W., & Meng, X. (2022c). A weighted mean temperature (Tm) augmentation method based on global latitude zone. *GPS Solutions, 26*, 141.
Yao, Y., Zhang, S., & Kong, J. (2017). Research progress and prospect of GNSS space environment science. *Acta Geodaetica Et Cartographica Sinica., 46*(10), 1408–1420.
Yu, S., Wan, R., & Fu, Z. (2016). Application of algebraic reconstruction technique on the GNSS water vapor tomography. *Geomatics and Information Science of Wuhan University., 41*(8), 1113–1117.
Zhang, S., Ye, S., Wan, R., & Chen, B. (2008). Preliminary tomography spatial wet refractivity distribution based on Kalman filter. *Geomatics and Information Science of Wuhan University., 33*(8), 796–799.
Zhang, W., Lou, Y., Liu, W., Huang, J., Wang, Z., Zhou, Y., & Zhang, H. (2020). Rapid troposphere tomography using adaptive simultaneous iterative reconstruction technique. *Journal of Geodesy., 94*, 76.
Zhao, Q., Liu, Y., Yao, W., & Yao, Y. (2021). Hourly rainfall forecast model using supervised learning algorithm. *IEEE Transactions on Geoscience and Remote Sensing., 60*, 4100509.
Zhao, Q., Yao, Y., Cao, X., & Yao, W. (2018). Accuracy and reliability of tropospheric wet refractivity tomography with GPS, BDS, and GLONASS observations. *Advances in Space Research., 63*(9), 2836–2847.
Zhao, Q., Zhang, K., Yao, Y., & Li, X. (2019). A new troposphere tomography algorithm with a truncation factor model (TFM) for GNSS networks. *GPS Solutions, 23*, 64.

Publisher's Note